Effect of self-consistent magnetic field on plasma sheet penetration to the inner magnetosphere: Rice convection model simulations combined with modified Dungey force-balanced magnetic field solver

Matina Gkioulidou,[1] Chih-Ping Wang,[1] and Larry R. Lyons[1]

Received 5 May 2011; revised 22 September 2011; accepted 24 September 2011; published 14 December 2011.

[1] Transport of plasma sheet particles into the inner magnetosphere is crucial to the development of the region 2 (R2) field-aligned current system (FAC), which results in the shielding of the penetration electric field and the formation of subauroral polarization streams (SAPS) and the Harang reversal, phenomena closely associated with storms and substorms. In addition to the electric field, this transport is also strongly affected by the magnetic field, which changes with plasma pressure and is distinctly different from the dipole field in the inner plasma sheet. To determine the feedback of force-balanced magnetic field to the transport, we have integrated the Rice convection model (RCM) with a modified Dungey magnetic field solver to obtain the required force balance in the equatorial plane. Comparing our results with those from a RCM run using a T96 magnetic field, we find that transport under a force-balanced magnetic field results in weaker pressure gradients and thus weaker R2 FAC in the near-Earth region and weaker shielding of the penetration electric field. As a result, plasma sheet protons and electrons penetrate farther earthward, and their inner edges become closer together and more azimuthally symmetric than in the T96 case. The Harang reversal extends farther dawnward, and the SAPS become more confined in radial and latitudinal extents. The magnitudes of azimuthal pressure gradient, the inner edges of thermal protons and electrons, the latitudinal range of the Harang reversal, and the radial and latitudinal widths of the SAPS from the force-balanced run are found to be more consistent with observations.

Citation: Gkioulidou, M., C.-P. Wang, and L. R. Lyons (2011), Effect of self-consistent magnetic field on plasma sheet penetration to the inner magnetosphere: Rice convection model simulations combined with modified Dungey force-balanced magnetic field solver, *J. Geophys. Res.*, *116*, A12213, doi:10.1029/2011JA016810.

1. Introduction

[2] The plasma sheet is a major plasma and energy storage region in the Earth's magnetosphere, and transport of plasma sheet particles into the near-Earth magnetosphere is important for setting up the plasma and electric and magnetic field conditions that lead to major geomagnetic disturbances, such as storms and substorms. It is thus of great importance to understand the underlying transport processes that govern the development of the plasma sheet and its structure.

[3] Plasma sheet particles moving toward the Earth under an enhanced convection electric field give rise to plasma pressure enhancements, which are associated with changes in magnetic field in maintaining force balance. The pressure changes cause changes in perpendicular current in the plasma sheet and eventually perpendicular current divergence, which requires a closure in the ionosphere through field-aligned currents (FAC). These FAC, referred to as the region 2 (R2) FAC, are responsible for electrodynamical coupling between magnetosphere and ionosphere, and the FAC intensity is determined mainly by the azimuthal gradient of plasma pressures and the radial gradient of magnetic flux tube volumes [*Vasyliunas*, 1970]. In order to maintain current continuity in the ionosphere, the FAC lead to modification of the convection electric field in the ionosphere. The modified electric field maps back into magnetosphere through equipotential mapping into the magnetosphere, which in turn affects the plasma sheet transport itself to the near-Earth region.

[4] Using the Rice convection model (RCM) with non-force-balanced Tsyganenko 96 (T96) magnetic fields, we have previously investigated [*Gkioulidou et al.*, 2009] how the electrodynamic feedback to the transport through the R2 FAC is responsible for the formation of the Harang reversal and the subauroral polarization streams (SAPS), which have been found to be closely associated with substorms and storms [*Zou et al.*, 2009; *Bristow and Jensen*, 2007; *Nishimura et al.*, 2008; *Anderson et al.*, 2001]. Since

[1]Department of Atmospheric and Oceanic Sciences, University of California, Los Angeles, California, USA.

0148-0227/11/2011JA016810

plasma sheet transport and FAC are also strongly affected by the magnetic field, which is found to be distinctly different from dipole in the inner plasma sheet [*Cahill*, 1966], feedback between the plasma transport and magnetic field is also essential to the R2 coupling. Therefore, in order to quantitatively determine inner magnetosphere plasma transport, it is necessary to self-consistently model plasma, electric and magnetic fields altogether.

[5] In recent years there has been an ongoing effort in the community for modeling the self-consistent feedback between plasma and magnetic field in the magnetosphere. *Wang et al.* [2003, 2004] created force-balanced magnetic fields for simulated plasma sheet plasma pressures around the midnight meridian by adding adjustable currents to the T96 magnetic fields. Using the Euler potentials method, *Zaharia et al.* [2004] and *Zaharia* [2008] established a magnetic field model that can provide 3-D force-balanced magnetic fields with a given pressure distribution by numerically solving the force balance equation. This model was later coupled with the Ring Current Atmosphere Interaction Model (RAM) [*Jordanova et al.*, 2010] to obtain magnetic fields in force balance with ring current pressures. Similarly, *Liu et al.* [2006] developed a force-balanced magnetic field solver using Euler potentials method for a modified Dungey magnetic field. The solver has been coupled with a ring current model based on the work of *Chen et al.* [1994] to simulate transport of storm time ring current ions under force-balanced magnetic field by numerically solving force balance equation in the equatorial plane. These simulations showed that magnetic field becomes more stretched to balance increasing plasma pressure and results, in turn, in less earthward penetration of particles and lower near-Earth pressures. However, self-consistent electric field is not taken into account in the above models.

[6] Self-consistent modeling of both electric and magnetic fields has been achieved by incorporating the RCM with a magnetic field relaxation technique developed by *Hesse and Birn* [1993] to simulate the near-Earth magnetosphere under enhanced convection [*Toffoletto et al.*, 1996, 2001; *Lemon et al.*, 2004; *Yang et al.*, 2010].

[7] The objective of this study is, by self-consistently modeling plasma, electric and magnetic fields, to examine how the R2 coupling, and as a result the penetration of the plasma sheet into the inner magnetosphere, is affected by the self-consistent magnetic field. For this objective, we have substituted the non-force-balanced T96 magnetic field used in our previous RCM simulations [*Gkioulidou et al.*, 2009] with force-balanced magnetic field provided by the modified Dungey force-balanced magnetic field solver mentioned above [*Liu et al.*, 2006; *Schulz and Chen*, 2008] to achieve 2-D force balance in the equatorial plane. The main reason for choosing this solver is its capability for efficient computation of magnetic field that exhibits the important features of magnetic local time (MLT)-dependent field line stretching, despite the tradeoff of being less accurate in its force balance in the z direction than a 3-D force balance model. Additionally, the solver's scheme for solving the force balance equation is relatively stable numerically, so that the solver can easily find a solution. Another advantage of our coupled model is that we have included realistic MLT-dependent particle boundary conditions based on Geotail statistical data that are a mixture of a cold population coming from the flanks and a hot one coming from the tail. Different from other studies that have focused mainly on the effects of self-consistent magnetic field on storm time ring current strength, we focus on how the feedback of magnetic field affects the R2 FAC and the penetration of the plasma sheet protons and electrons to the near-Earth region, and how this eventually affects the structure of the convection electric field, including the Harang reversal and SAPS, in the inner magnetosphere.

[8] The details of our coupled model, including the magnetic field solver, are described in section 2. In section 3.1 we show main features of the self-consistent magnetic field model and compare it with statistical THEMIS-Geotail observations. We then investigate the effect of the self-consistent magnetic fields on plasma pressure distributions in section 3.2, and on plasma sheet proton and electron inner edges in section 3.3. On the basis of the results of the sections 3.2 and 3.3, we explain in section 3.4 how the plasma sheet transport simulated in self-consistent magnetic field can affect the Harang reversal and SAPS. Comparisons are made with previous published observational results where feasible, and detailed comparison with observations of the spatial distributions of ion and electron populations from the midtail to inner magnetosphere is given in the companion paper [*C.-P. Wang et al.*, 2011] (hereinafter Paper 2).

2. Model

2.1. Rice Convection Model

[9] The RCM [*Toffoletto et al.*, 2003] calculates the bounce–averaged electric and magnetic drift of a flux tube filled with an isotropic distribution of ions or electrons under the assumption of slow-flow approximation within a self-consistently computed electric field. The assumption of isotropy is reasonable, since, as can be seen in Figure 4 of Paper 2, plasma is quite isotropic in the plasma sheet.

[10] For an isotropic particle distribution the particle kinetic energy change can be simply determined by the change in flux tube volume according to the relation $E_k = \lambda V^{-2/3}$ [*Wolf*, 1983], where λ is constant along a particle's drift path and is called the energy invariant, V is the flux tube volume. The bounce-averaged drift velocity $\mathbf{V}_D$ of particles of a given energy invariant λ at position $\mathbf{x}$ and time t can then be described as

$$\mathbf{V}_{\mathrm{D}}(\mathbf{x},t) = \frac{\mathbf{B}(\mathbf{x},t)\times\nabla\Phi(\mathbf{x},t)}{|B(\mathbf{x},t)|^2} + \frac{\mathbf{B}(\mathbf{x},t)\times\lambda\nabla V(\mathbf{x},t)^{-2/3}/q}{|B(\mathbf{x},t)|^2}. \quad (1)$$

The RCM traces the drift trajectory of particles of different λ within a flux tube using (1) with given electric potential $\Delta\Phi(\mathbf{x}, t)$ and $V(\mathbf{x}, t)$. The RCM grid is specified in the ionosphere, so $\mathbf{B}$ in equation (1) is the magnetic field in the ionosphere. The spatial distributions of plasma density n and pressure P for each species are obtained from the flux tube content $\eta(\mathbf{x}, \mathrm{t})$, that is the number of particles per unit magnetic flux, by the relations

$$n(\mathbf{x},t) = \sum_j \frac{\eta_j(\mathbf{x},t)}{V(\mathbf{x},t)} \qquad P(\mathbf{x},t) = \frac{2}{3}\sum_j \frac{\eta_j(\mathbf{x},t)}{V(\mathbf{x},t)}\lambda_j V(\mathbf{x},t)^{-2/3}, \quad (2)$$

where the subscript j is the index of the energy channel. Temperature T can be obtained from P/nk_B where k_B is Boltzmann's constant.

[11] The RCM includes magnetosphere-ionosphere coupling through field-aligned currents, which can be computed by the Vasyliunas equation [*Vasyliunas*, 1970]. The self-consistent electric field is obtained by satisfying current continuity both in magnetosphere and ionosphere, namely,

$$\nabla_i \cdot [\Sigma \cdot (\nabla_i \Phi_i)] = -j_{\parallel} \sin(I) = -\frac{B_i}{2B} \hat{b} \cdot \nabla V \times \nabla P \sin(I), \quad (3)$$

where Σ is the field line–integrated conductivity tensor, I is the dip angle of the magnetic field in the ionosphere, and $j_{\parallel}$ is the ionospheric field-aligned current density of the northern or southern hemisphere (north–south symmetry is assumed). Index i refers to ionosphere-computed quantities.

[12] With given Σ and boundary conditions at the high- and low-latitude boundary, (3) can be solved to obtain electric potential Φ_i. The conductivity tensor Σ includes both the Hall and Pedersen conductivities. The conductance includes Solar-EUV-generated conductance that is estimated from the IRI-90 empirical ionosphere driven by F10.7 and the *Ap* index, and auroral conductance, which, in this study, is estimated using the electron precipitation from the simulated plasma distributions, assuming 1/3 of strong pitch angle scattering and the algorithm of *Robinson et al.* [1987]. The high-latitude boundary condition for the potential is a Dirichlet boundary condition; the overall strength of convection is determined by setting the total range of potential on the boundary equal to the polar cap potential $\Delta\Phi_{PC}$. A two-cell convection pattern is assigned to describe the electric potential inside the polar cap. The low-latitude boundary condition incorporates the effects of the equatorial electrojet. Note that the RCM includes the contribution to the electric field in the magnetospheric equatorial plane from the induced electric field when time-changing magnetic fields are used for the mapping.

2.2. Plasma Boundary Conditions

[13] The location of the outer boundary is specified as a 15 R_E circle (the center of the circle is at $X = -5$ R_E and $Y = 0$) in the equatorial plane that reaches $X = -20$ R_E at midnight and $|Y| = 15$ R_E at dawn and dusk. The latitudes in the ionosphere that map to the outer boundary vary as magnetic field changes. The inner boundary is at $r \sim 2$ R_E. Along the outer boundary, the proton and electron distributions at different MLT are established from a fitting of two-component kappa distributions, which are a combination of cold and hot populations, to statistical results from 11 years of Geotail observations under southward and northward interplanetary magnetic field (IMF) conditions [*Wang et al.*, 2007; *Gkioulidou et al.*, 2009]. In this paper we used the southward IMF boundary condition for $N_{SW} < 6.5$ cm^{-3}, $V_{SW} < 400$ km/s, $|B_{zIMF}| < 1.3$ nT [see *Gkioulidou et al.*, 2009, appendix Table 3].

2.3. Modified Dungey Force-Balanced Magnetic Field Solver

[14] In order to provide the RCM with self-consistent magnetic fields, we use a force balance solver [*Liu et al.*, 2006; *Schulz and Chen*, 2008] to obtain magnetic fields that are in force balance with given plasma pressures in the equatorial plane. When in equilibrium, magnetic field and plasma pressure satisfy the force balance equation:

$$\mathbf{J} \times \mathbf{B} = \nabla P, \quad (4)$$

where P is the isotropic pressure, and $\mathbf{B}$ is magnetic field and $\mathbf{J} = \nabla \times \mathbf{B}/\mu_o$ is current density.

[15] The magnetic field $\mathbf{B}$ can be expressed in terms of two Euler potentials [*Stern*, 1967] as

$$\mathbf{B} = \nabla\alpha \times \nabla\varphi, \quad (5)$$

where

$$\alpha = \partial\Phi_B/\partial\varphi = -\mu_E/L \quad (6)$$

is the magnetic flux per unit magnetic local time (MLT), Φ_B is the magnetic flux, φ is MLT, μ_E is the geomagnetic dipole moment, and L is the dimensionless label of the field line.

[16] In our solver we make two important assumptions. The first assumption is the fact that our second Euler potential is the azimuthal angle φ. This means that each magnetic field line always lie in the same meridian plane. Therefore, our solver does not account for azimuthal perturbations of the magnetic field. Observations inside $r = 8$ R_E [*Le et al.*, 2004] indicate the perturbations from FAC are too small to result in substantial bending, and magnetic field from the T96 also indicate strong field lines bending only occurs in regions very close to the magnetopause.

[17] The second assumption is that the field lines satisfy the Dungey field line function:

$$L = r\left[\left(1 + \frac{r^3}{2b^3}\right)\sin^2\theta\right]^{-1} = r_0\left[\left(1 + \frac{r_0^3}{2b^3}\right)\right]^{-1}, \quad (7)$$

where θ is magnetic colatitude and r_0 is radial distance from the point dipole at the equator in R_E, The parameter b represents field line stretching, and it is a function of both radial distance and MLT but remains constant along each field line. We should note here that the original Dungey model [*Dungey*, 1963] assumes a dipolar $\mathbf{B}$ field plus a uniform "southward" perturbation $\Delta\mathbf{B}$ parallel to the magnetic dipole axis, that is, the stretching parameter b is constant and the model is current-free. Our solver allows b to vary from field line to field line to accommodate current, and is thus able to produce the required $\mathbf{J} \times \mathbf{B}$ to balance the pressure gradient force. For the rest of the paper we refer to our solver as the modified Dungey solver.

[18] With the first assumption, $\mathbf{B}$ can be expressed in spherical coordinates as a function of the partial derivative of α with respect only to geocentric radial distance r and colatitude θ:

$$\mathbf{B}(r,\theta) = \nabla\alpha \times \nabla\varphi = \hat{r}\frac{\partial\alpha/\partial\theta}{r^2\sin\theta} - \hat{\theta}\frac{\partial\alpha/\partial r}{r\sin\theta}, \quad (8)$$

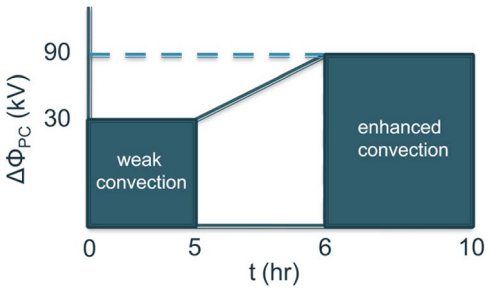

Figure 1. Schematic illustrating the polar cap potential drop ($\Delta\Phi_{PC}$) change with time in our simulation runs.

which means that the curl of $\mathbf{B}(r, \theta)$ can be expressed as

$$\nabla \times \mathbf{B} = \hat{r}\frac{\partial^2\alpha/\partial r\partial\varphi}{r^2\sin^2\theta} + \hat{\theta}\frac{\partial^2\alpha/\partial\theta\partial\varphi}{r^3\sin^2\theta} - \frac{1}{r}\hat{\varphi}\left[\frac{\partial^2\alpha/\partial^2 r}{\sin\theta} + \frac{1}{r^2}\frac{\partial}{\partial\theta}\left(\frac{\partial\alpha/\partial\theta}{\sin\theta}\right)\right]. \quad (9)$$

[19] With the second assumption of using the Dungey field line equation (7), all the partial derivatives of α on the right-hand side of (9) can be converted into partial derivatives of α with respect to r_0 only at the equator, so that azimuthal current density at the equator becomes

$$\frac{\left[(\nabla\times\boldsymbol{B})_\varphi\right]_0}{\mu_0} = -\hat{\varphi}\frac{1}{r_0\mu_0}\left[\frac{\partial^2\alpha}{\partial r_0^2} - \frac{2\alpha}{3\mu_E + 2r_0\alpha}\frac{\partial\alpha}{\partial r_0}\right], \quad (10)$$

where the subscript 0 refers to quantities at the equatorial plane.

[20] Therefore, given the above two assumptions, the 3-D force balance equation (4) is reduced to a 2-D problem that requires solving two ordinary differential equations, the radial and azimuthal components of force balance in the equatorial plane:

$$-\frac{\left[(\nabla\times\mathbf{B})_\varphi\right]_0}{\mu_0}B_0 = \frac{\partial P_0}{\partial r_0} \quad (11)$$

$$\frac{\left[(\nabla\times\mathbf{B})_r\right]_0}{\mu_0}B_0 = \frac{1}{r_0}\frac{\partial P_0}{\partial\varphi}. \quad (12)$$

[21] The azimuthal component has an analytical solution, namely,

$$\frac{B_0^2}{2\mu_0} + P_0 = P_{total}(r_0). \quad (13)$$

Equation (13) actually implies that the sum of magnetic and plasma perpendicular pressure in the equatorial plane is the same along the same radial distance circle.

[22] Combining equations (6) and (10), the radial component of the force balance equation (11) becomes a second-order ordinary nonlinear differential equation in $1/L$ with respect to r_0, namely,

$$\frac{\partial^2(1/L)}{\partial r_0^2} = \left(-\frac{2}{\mu_0 P_{norm}(3L-2r_0)} - \frac{\partial\ln P_{norm}}{\partial r_0} + \frac{2}{r_0}\right) \cdot \left(\frac{\mu_0 P_{norm}}{1+2\mu_0 P_{norm}}\right)\frac{\partial(1/L)}{\partial r_0}, \quad (14)$$

where $P_{\mathrm{norm}} = P_0/B_0^2$ and B_0 is the magnetic field at the equator. Therefore, for a given plasma pressure distribution in the equatorial plane, force balanced magnetic field can be obtained by numerically solving equation (14) with boundary conditions for $1/L$, and $\partial(1/L)/\partial r_0$ specified at 2 R_E, which is our inner boundary, satisfying at the same time the condition of equation (13) for the same radial distance. The fact that the stretching parameter b does not appear in the equations (13) and (14)) is because we have explicitly used the Dungey field line equation (7), and thus b, to express all the partial derivatives of $1/L(r, \theta)$ at the equator only as partial derivatives of $1/L$ with respect to r_0. To compute the flux tube volume which is used in the bounce-averaged equation of particle motion as well as in field-aligned current (FAC) calculation in the RCM, we use *Schulz and Chen* [2008, equation (1)] and that equation's two required inputs, $b(r_0, \varphi)$ and $\partial b/\partial r_0$, can be simply obtained with equation (7).

2.4. The RCM With Self-Consistent Magnetic Field

[23] By combining the RCM with the modified Dungey solver, we can conduct simulations under both self-consistent electric and magnetic fields. For this study, we ran the self-consistent simulation first with constant cross polar cap potential drop ($\Delta\Phi_{PC}$) of 30 kV for 5 simulation hours (t = 5 h), and then gradually, within an hour, increased $\Delta\Phi_{PC}$ to 90 kV (t = 6 h) and kept it constant for another 4 h (t = 10 h). Figure 1 shows a schematic diagram of the time-dependent $\Delta\Phi_{PC}$ change in our run. Every 10 min the magnetic field was updated so that it maintains force balance with the RCM pressures at all time. The plasma boundary condition that was described in section 2.2 remains constant throughout the simulation. For the two magnetic field boundary conditions, $1/L$ and $\partial(1/L)/\partial r_0$ at 2 R_E, we used dipole values for $1/L$ at all MLT but adjusted $\partial(1/L)/\partial r_0$ at each MLT to achieve the best overall force balance both radially and azimuthally.

[24] There are some limitations in our current coupled model. The force balance is calculated only in the equatorial plane, thus balance in the off-equatorial region is not achieved perfectly. Since b is constant along each field line, the magnetic field lines are constrained to a "Dungey field line" shape. Also, no outer boundary conditions for the magnetic field solver are specified to include the effect of the magnetopause. Despite the above limitations, the modified Dungey solver is capable of describing the important features of field line stretching according to equatorial pressure profiles and the fields can be numerically computed rather efficiently. Therefore, the coupled RCM-modified Dungey solver model allows us to more accurately evaluate

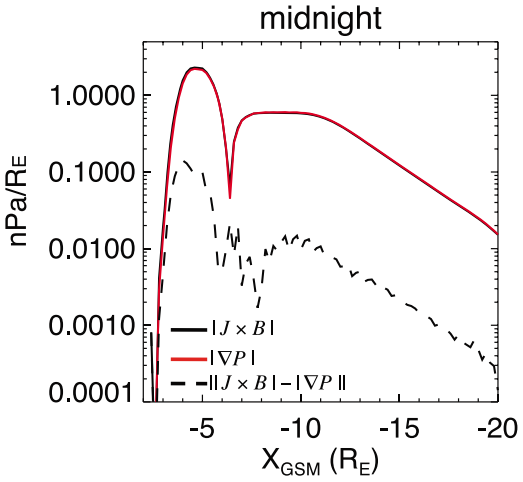

Figure 2. Radial profile along the midnight axis of $|\mathbf{J} \times \mathbf{B}|$ (solid line), $|\nabla P|$ (red line), and $||\mathbf{J} \times \mathbf{B}| - |\nabla P||$ (dashed line) at $t = 10$ h.

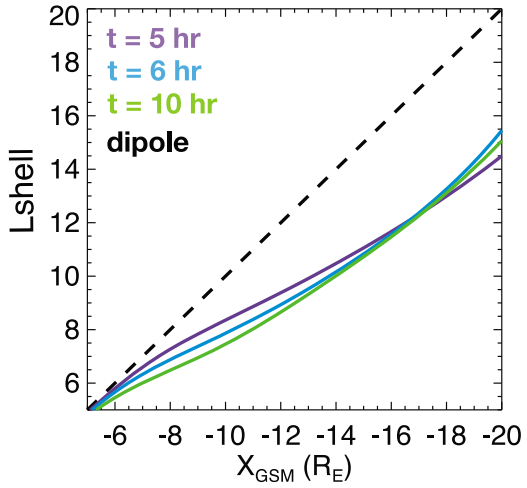

Figure 4. Radial profile of L shell at the equator at midnight for $t = 5$ h (purple line), $t = 6$ h (blue line), and $t = 10$ h (green line).

how the self-consistent feedback between plasma and magnetic field affects the electromagnetic coupling between the magnetosphere and ionosphere that is crucial to the penetration of the plasma sheet into the inner magnetosphere.

3. Simulation Results

3.1. Self-Consistent Magnetic Field

[25] First of all, we checked that our magnetic field is indeed in force balance with the plasma pressure at a given time. In Figure 2 we have plotted $|\mathbf{J} \times \mathbf{B}|$ (solid line), $|\nabla P|$ (red line) and the absolute value of their difference (dashed line) versus radial distance at the equator along the midnight meridian, at $t = 10$ h, that is, 4 h after $\Delta\Phi_{PC}$ was increased to 90 kV. Apart from the region $-2 < X\_GSM < -3$, where there is no plasma pressure because particles from the boundary cannot reach that region, the difference between the two forces throughout the simulation domain is clearly negligible comparable to the two forces, indicating that we have achieved satisfactory force balance.

[26] In Figure 3 we show the magnetic field lines at midnight, also at $t = 10$ h. The modified Dungey field lines are shown with solid lines while the corresponding dipole field lines are shown with dashed lines. Different colors correspond to different L shells. We can clearly see the Dungey field line shape mentioned above, but also the stretching of the field lines in comparison to the dipole ones.

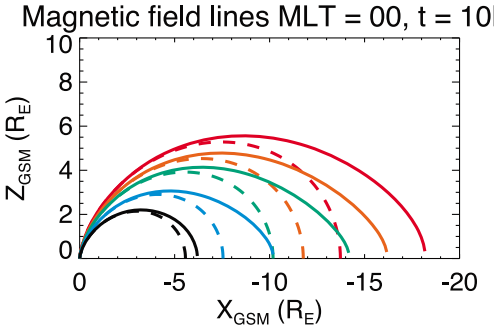

Figure 3. Magnetic field lines for dipole (dashed lines) and modified Dungey (solid lines) magnetic field models at midnight for $t = 10$ h. Different colors represent different L shells.

[27] In order to show the amount of stretching of the field lines, in Figure 4 we have plotted the radial profile of L shells at the equator at midnight for $t = 5$ h (purple), $t = 6$ h (light blue) and $t = 10$ h (green). Going from weak (30 kV) to enhanced convection (90 kV), we see more stretching in the inner magnetosphere (lower L shells for the same radial distance) but less stretching toward the tail. In the regions earthward (tailward) of the peak of the duskward cross-tail current, the perturbation of the magnetic field caused by this the current is negative (positive). Therefore, as the duskward current increases with increasing convection, magnetic field gets more (less) stretched in the inner (outer) magnetosphere.

[28] One of the major advantages of using a self-consistent magnetic field model is its ability to produce a dawn-dusk asymmetric magnetic field according to the plasma pressure gradients, which, as is discussed later, plays an important role in magnetosphere-ionosphere coupling. Figure 5 shows the equatorial profiles of plasma pressure, B_z, and L shell along the dawn (yellow line) and dusk (purple line) meridians at $t = 6$ h (convection just reached 90 kV). The dipole field (dashed line) is also plotted as a reference. At dusk, where the pressure is higher than at dawn, the magnetic field lines are more stretched and B_z is smaller in the inner magnetosphere.

[29] To investigate if the above changes with increasing convection seen in our self-consistent (SC) magnetic field configuration are reasonable, we compare them with statistical values of magnetic field from Geotail and THEMIS. In Figure 6 we plot radial profiles of $V^{-2/3}$ (Figure 6, top) and B_z (Figure 6, bottom) at midnight for our SC magnetic field (red line), and for the data (solid line corresponds to the median, while the minimum and maximum of the error bar indicate the 25% and 75% percentiles, respectively). The simulations results are for $t = 5$ h, that is, under weak convection of 30 kV (Figure 6, left) and for $t = 6$ h, that is, right after convection has reached 90 kV (Figure 6, right). The

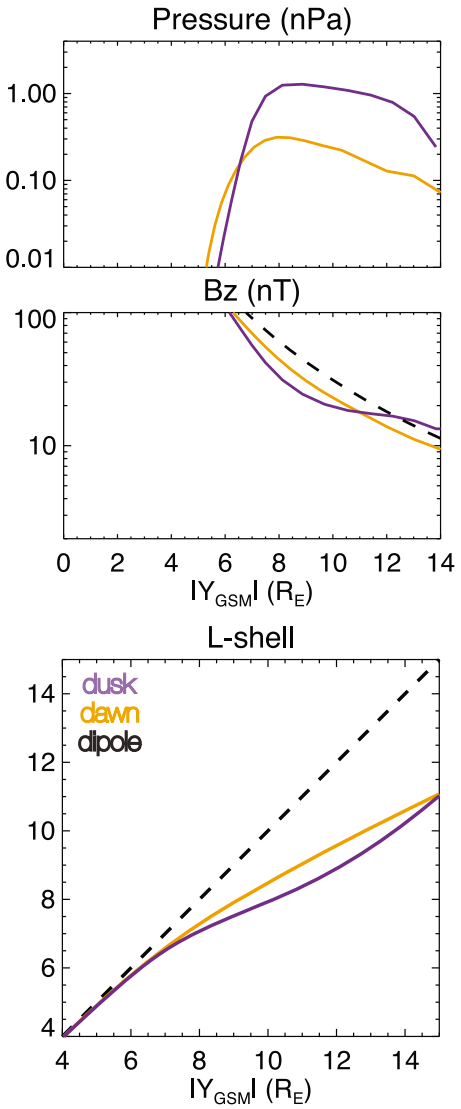

Figure 5. Equatorial profiles of plasma pressure, B_z, and L shell along the dawn (orange line) and dusk (purple line) meridians at t = 6 h under enhanced convection (90 kV). Dipole field (dashed line) is also plotted as a reference.

Geotail and THEMIS data have been sorted out into 2 different convection levels with low AE values: (1) weak convection: $20 < \Delta\Phi_{PC} < 40$ kV, $10 < AE < 50$ nT and (2) strong convection: $50 < \Delta\Phi_{PC} < 100$ kV, $50 < AE < 150$ nT. We included the additional criteria based on AE, indicated above, to minimize effects from the substorm expansion phase. We would like to point out that the model comparison with observations is not rigorous since the temporal variation of the convection and particle conditions for our simulation is rather simple compared with the more complicated conditions that correspond to the statistical results. Therefore, here we focus more on whether our self-consistent magnetic field model can reproduce the trends of the changes seen in the data. We can see that, the $V^{-2/3}$ of the SC run has in general good agreement with observations, although the modeled values are higher than the observed ones from $r \sim 8$–15 R_E. Note that $V^{-2/3}$ is the parameter related to the magnetic field that is actually used in the RCM calculations of bounce-averaged drift and FAC. The method of obtaining V from observations is discussed in Paper 2. The comparison of B_z with observations, on the other hand, is not as good. Our self-consistent B_z has, in general, larger values than the observed one. The discrepancy between observed and modeled values of both B_z and $V^{-2/3}$ has partially to do with the fact that we do not consider force balance in the z direction, due to our restriction to the Dungey field line shape, which limits the degree of stretching that is attainable. In addition, concerning the B_z values, the spacecraft measurements, as opposed to the simulated ones, were taken in the vicinity of the equatorial plane, not exactly at the center of the current sheet (where B_x and B_y are zero). The limitation to the stretching would mean that our mapping to magnetosphere might not be exact. However, the self-consistent B_z exhibits a slight increase toward the tail with enhanced convection (dashed lines indicate B_z = 10 nT for reference), which is consistent with the observational trend. This is also due to the different effect on the stretching of the magnetic field earthward and tailward of the duskward current's peak, as discussed earlier (see description of Figure 4).

3.2. Effect of the Self-Consistent Magnetic Field on Plasma Pressure Distributions

[30] As pressure evolves as a result of particle transport, magnetic field also changes to maintain force balance, which directly changes magnetic drift transport as well as FAC. The changing FAC modifies electric drift through coupling with the ionosphere, which changes particle transport in turn. To investigate how the feedback from magnetic field affects the plasma sheet dynamics and the resulting plasma and field distributions, we compare our current SC RCM runs with force-balanced magnetic field with results from our previous simulations [*Gkioulidou et al.*, 2009] under specified non-force-balanced, dawn-dusk symmetric Tsyganenko 96 (T96) [*Tsyganenko*, 1995, 1996] magnetic field. All the setup for $\Delta\Phi_{PC}$ and boundary conditions in the two runs are exactly the same; the only difference is the magnetic field. To get the T96 magnetic field values, as in the work of *Gkioulidou et al.* [2009], we decrease the IMF B_z from 0 to −7 nT and *Dst* from −10 nT to −11 nT when the $\Delta\Phi_{PC}$ increases from 30 to 90 kV (IMF B_z and *Dst* are used as an input for the T96), and two other inputs, Pdyn = 1.7 nPa and IMF B_y = 0, for the T96, are kept constant throughout the simulation. Since the T96 magnetic field is not in force balance with the simulated plasma pressure, we chose the above values for the T96 parameters in order to give typical magnetic field configurations for weak and for enhanced convection conditions. The relationship between IMF B_z reduction and $\Delta\Phi_{PC}$ drop change is based on *Weimer* [1995, equation (6)]. We decrease *Dst* only by 1 nT because the ring current developed in our simulation, even after 5 h, is not strong enough to justify a significant drop on the *Dst* index (note that we have not used initial plasma conditions that would account for a preexisting ring current in the inner magnetosphere, so that we can purely investigate the plasma sheet transport from the boundary all the way to the inner magnetosphere).

[31] In Figure 7 we show FAC and pressure profiles mapped to the equatorial plane (Figure 7, top) as well as FAC and Pedersen conductivity profiles in the ionosphere (Figure 7, bottom) at t = 10 h, that is, 4 h after constant 90 kV

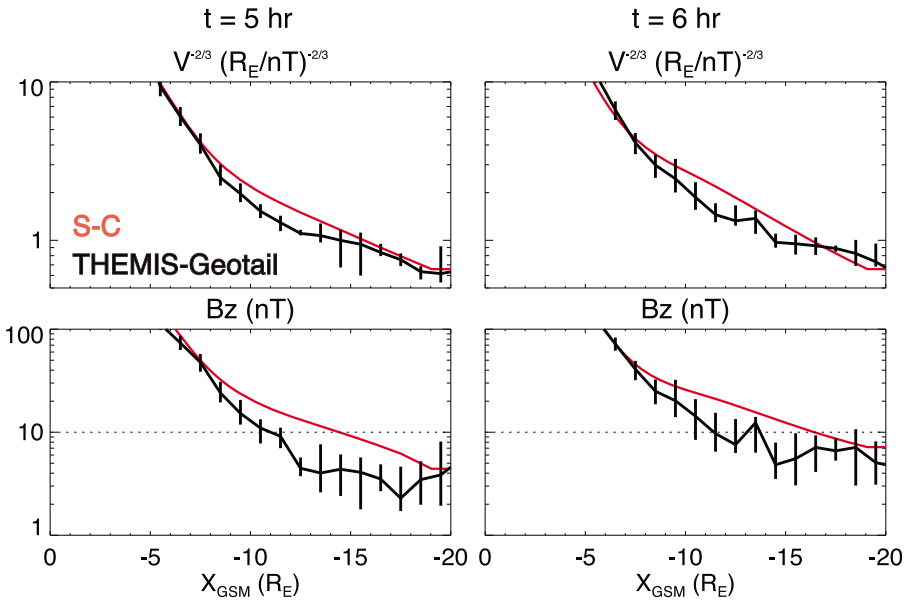

Figure 6. Radial profiles of (top) $V^{-2/3}$ and (bottom) B_z, at midnight, for self-consistent magnetic field (red line) and THEMIS-Geotail statistical data (solid line corresponds to the median, while the minimum and maximum of the error bar indicate the 25% and 75% percentiles, respectively), under (left) weak convection and (right) enhanced convection. Dashed lines indicate B_z = 10 nT for reference.

enhanced convection, under self-consistent (Figure 7, left) and under T96 (Figure 7, right) magnetic fields. The reason we show the above properties for t = 10 h is that, by that time, the changes in our simulation results are insignificant which means that our simulation has essentially reached equilibrium. The line contours in all the plots are equipotentials. We also plotted electric field vectors (arrows) at the equatorial plane in the nightside region on top of the FAC profiles.

[32] We see that, in the SC run, compared to the T96 run, we have lower pressure in the inner magnetosphere and weaker dawn-dusk pressure asymmetry. Figure 8 shows azimuthal pressure profiles (Figure 8, top) and pressure gradients (Figure 8, middle) at r_0 = 9–12 R_E under weak convection (t = 5 h) from the two simulation runs. The pressure gradients from the SC results are mainly duskward gradients (negative values); the T96 results, on the other hand, have a pressure peak near midnight MLT, thus resulting in duskward (dawnward) gradients at the postmidnight (premidnight) MLT. Using pressures simultaneously measured by two THEMIS spacecraft that were at the same radial distance but slightly separated in MLT, *Xing et al.* [2009] showed that the azimuthal pressure gradients are mainly duskward at the nightside MLT with smaller magnitudes at the premidnight than postmidnight MLT, which is consistent with the SC results. Note that, by applying recent more accurate calibration of the THEMIS SST pressure, X. Xing (personal communication, 2011) found that the magnitudes of the pressure gradients are actually about half of the magnitudes shown by *Xing et al.* [2009, Figure 3], which brings the comparison with the SC results to better agreement. Additionally, Figure 8 (bottom) shows observed statistical equatorial azimuthal pressure profiles at the same radial distances under weak convection obtained from the analysis of THEMIS-Geotail observations in Paper 2. The statistical profiles also indicate relatively weak azimuthal gradients as seen in the SC results and no prominent pressure peak around midnight as seen in the T96 results.

[33] The effect of weaker azimuthal pressure gradients from the SC on the FAC and electric field distributions can be seen in Figure 7. The weaker azimuthal pressure gradients result in weaker R2 FAC (the pair of FAC at $X \sim -5$ to -10 R_E with downward FAC (in red) in the premidnight and upward FAC (in blue) in the postmidnight sector). The change in the R2 FAC modifies, in turn, electric field distributions through M-I coupling. We found that electric field becomes more dawn-dusk asymmetric under self-consistent magnetic field, with stronger electric field in the postmidnight sector than the premidnight one in the region beyond $X_{GSM} \sim -6$ R_E. Also, the radial and latitudinal extent of the strong electric fields in the near-Earth premidnight sector (latitude ~65° in the ionosphere and $X_{GSM} \sim -4$ R_E in the magnetosphere), also known as SAPS because of their strong westward **E** × **B** convection flow, become much more confined in latitudinal and radial extent than in the T96 run. The Harang reversal, the region of converging electric fields in the nightside ionosphere at auroral latitudes (60°–66°), extends further toward dawn in the SC results.

[34] In the next section we analyze in depth how particle transport under SC magnetic field results in the above different FAC and electric field distributions from those under fixed magnetic fields.

3.3. Effect of Self-Consistent Magnetic Field on Plasma Sheet Proton and Electron Inner Edge

[35] An important yet fundamental question arising from the above investigation of the plasma sheet properties is, how does applying a force-balanced magnetic field modify the plasma sheet particle transport to the inner

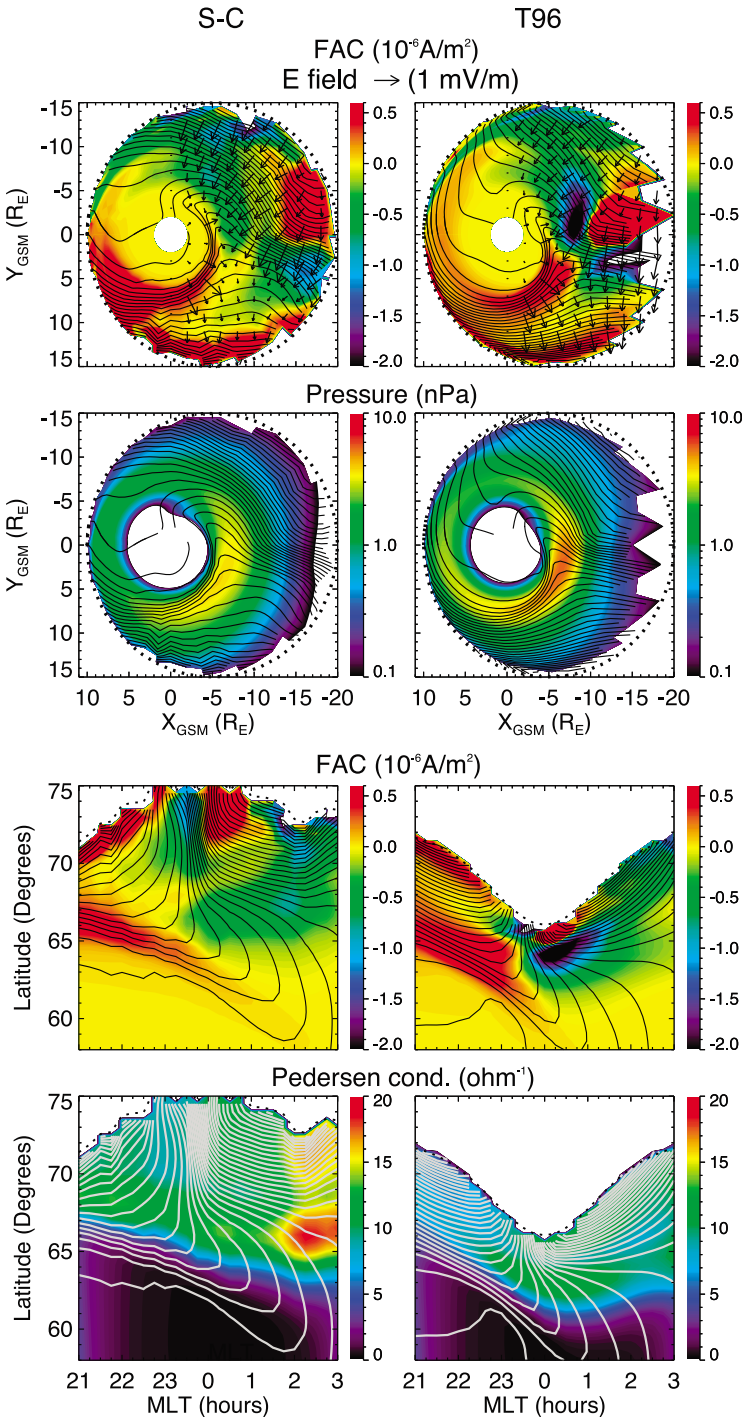

Figure 7. (top) Field-aligned currents (FAC) (blue for upward, red for downward) and pressure profiles mapped to the equatorial plane, as well as electric fields (arrows), and (bottom) FAC and Pedersen conductivity profiles in the ionosphere at t = 10 h under (left) self-consistent and (right) T96 magnetic fields.

magnetosphere relative to applying a non force-balanced magnetic field (namely, T96)?

[36] Figure 9 shows plasma sheet properties in the equatorial plane at t = 6 h (just after $\Delta\Phi_{PC}$ has increased to 90 kV), with the SC run (Figure 9, left) and T96 run (Figure 9, right). In all of Figure 9, a bold dotted line gives a circle at r = 10 R_E circle for reference. Figure 9a shows magnetic drift velocities (arrows) for thermal plasma sheet protons (5 keV at 20 R_E at midnight, ~100 keV at 6.6 R_E), pressure profile (color contours) and equipotentials (solid lines). As we can see, compared to the T96 run, using SC magnetic field results in weaker duskward magnetic drift for this thermal plasma sheet population, which is the main contributor to plasma pressure, thus leading to weaker azimuthal pressure gradient in the inner magnetosphere. The arrows in Figure 9b show the directions of ∇P and of ∇V,

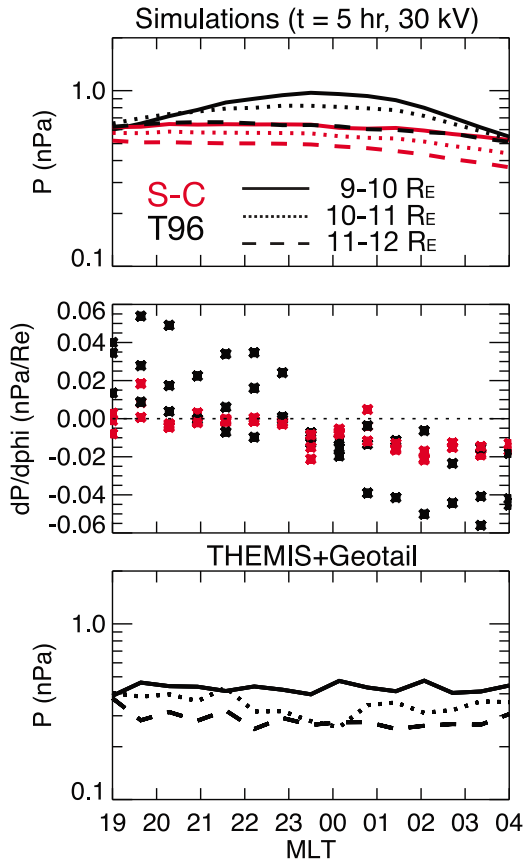

Figure 8. (top) Azimuthal pressure profile and (middle) pressure gradient using T96 (solid line) and self-consistent magnetic fields (red line), as well as (bottom) statistical THEMIS-Geotail azimuthal pressure profiles, for r_0 = 9–10 R_E (solid line), r_0 = 10–11 R_E (dotted line), and r_0 = 11–12 R_E (dashed line) under weak convection.

their magnitude being given by the arrow color. While in both runs ∇V is mainly in the radial direction, ∇P is also seen to be directed mainly radially only in the SC run (for the postmidnight region $X \sim -8$ to -10 R_E). Note that this is in agreement with results of *Zaharia* [2008] where he showed that, in a force-balanced magnetic field, the maximum angle between the pressure gradient and the field line curvature decreases with increasing plasma $\beta_0 = 2P_0/B_0^2$, that is, ∇P and ∇V become more aligned (antiparallel). As a result, the R2 FAC (color contours in Figure 9c), which depend on the cross product of pressure gradients and flux tube volume gradients (see equation (3)) are much weaker in the SC run and thus less efficient electric field shielding occurs in the near-Earth region, especially in the postmidnight sector, where the upward FAC is significantly weaker than in the T96 run, as can be seen by the equipotentials (solid lines in Figure 9c).

[37] Finally, Figure 9d shows electric drift with orange arrows (drift due to induced electric field is neglected), as well as thermal protons' magnetic drift with blue arrows, trajectories beyond 5 R_E with solid lines, partial pressure with shaded contours and inner edge with the red line (earthward of this red line the particle content, η, is less than 20% of the boundary value at midnight). Thermal protons' energy is the same as Figure 9a. In the postmidnight sector, in the SC run, the plasma sheet protons are affected more by electric drift than in the T96 run, and, therefore, they penetrate further earthward. The change in particle transport also changes particle distributions, as can be seen from the inner edge of thermal protons becoming more aligned with the radial circle. That inner edge is also well correlated with the inner edge of the partial pressure profile of the same energy protons. As a result of this postmidnight earthward penetration, the inner edge of the plasma sheet thermal protons is more dawn-dusk symmetric in the SC run, as compared to the much more pronounced dawn-dusk asymmetry in the T96 run.

[38] Given the above understanding of how different plasma sheet proton inner edges are obtained using SC magnetic field versus T96, we now investigate how the relative locations of plasma sheet protons' and electrons' inner edges are affected by the self-consistent magnetic field.

[39] Figure 10 shows equatorial inner edges of particle content for plasma sheet thermal energies (same as in Figure 9) protons (red line) and electrons (blue line) for the two runs under weak and enhanced convection. Circles at 8 R_E and 10 R_E are shown for reference. The comparisons show that the inner edges of protons and electrons in the SC run are closer to each other and more azimuthally symmetric than in the T96 run. Comparing weak convection with enhanced convection, the inner edges of both protons and electrons in the SC run become more azimuthally symmetric with increasing convection and become even closer to each other. Also, the intersection of the ion and electron edges moves duskward with enhanced convection. The inner edges in the SC run is in better agreement than in the T96 run with those seen in statistical particle distributions shown in Figure 7 of Paper 2. The locations of the inner edges and relative position between ion and electron edges play important roles in determining the characteristics of the Harang reversal and the SAPS.

3.4. Effect of Self-Consistent Magnetic Fields on the Harang Reversal and SAPS Region

[40] The earthward penetration of the plasma sheet strongly affects the spatial distribution of convection electric field in the near-Earth region, including the Harang reversal and the SAPS. In the recent years there has been a revival of the interest in these features since they seem to be closely associated with the two major geomagnetic disturbances, storms and substorms.

[41] As can be seen in Figure 7, the Harang reversal in our SC simulation under enhanced convection extends from ~66° to 60° latitudes. This is in agreement with the ionospheric SuperDARN observations by *Zou et al.* [2009], who found the latitudinal extent of Harang reversal during the growth phase of nine substorms varied between 67.5° and 62.5°.

[42] The ionospheric feature of the Harang reversal has been referred to as electric field skewing when mapped to magnetosphere. Observational evidence of this skewing has been shown in a paper by *Matsui et al.* [2010]. By statistically analyzing Cluster data, they found changes in the sign of the x component of the electric field in the postmidnight sector between the main and recovery phases of storms, which is likely due to the bending of the equipotentials in the

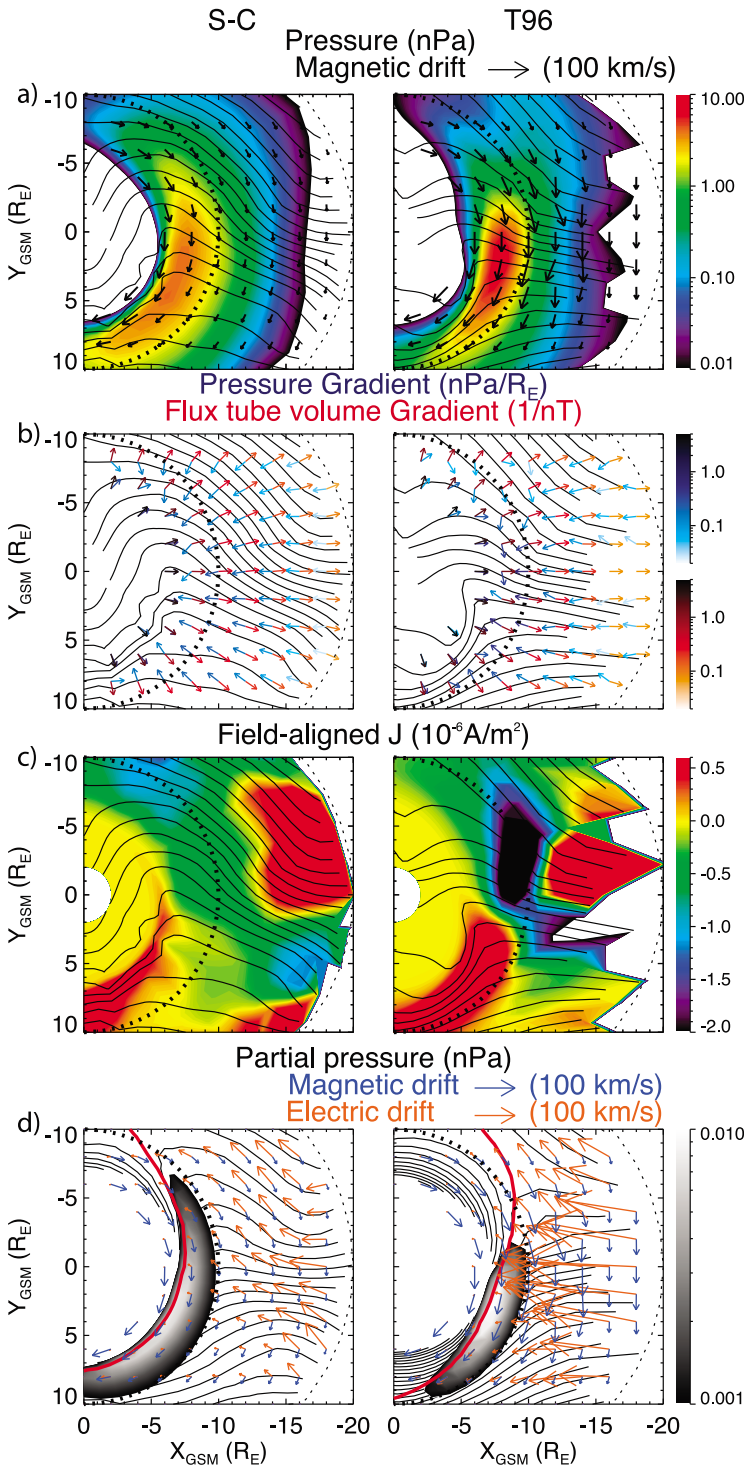

Figure 9. (a) Pressure with color contours, equipotentials with solid contours, and magnetic drift with arrows. (b) Unit vectors of ∇P with blue and ∇V with red, going from lighter to darker color with increasing magnitude; equipotentials are solid contours. (c) FAC with color contours (blue for upward, red for downward) and equipotentials with solid contours. (d) Magnetic drift of thermal protons (5 keV at 20 R_E at midnight) with blue arrows, electric drift with orange arrows, thermal protons' open trajectories (only beyond 5 R_E) with solid contours, thermal protons' inner edge with red line (the particle content, η, in the region inward of the red line is less than 20% of the boundary value at midnight), and partial pressure profile of the same energy protons with shaded contour. The bold dotted line in all the plots is the 10 R_E circle, and all the plots are for t = 6 h (convection has just reached 90 kV).

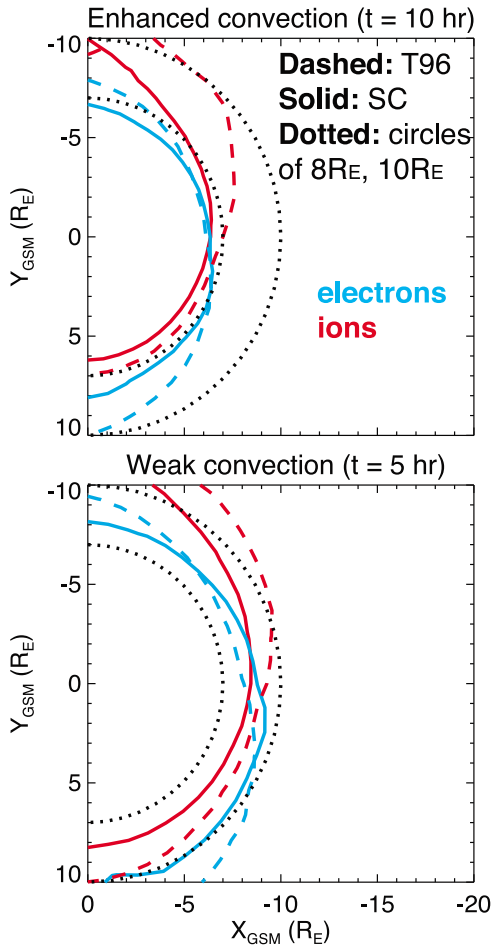

Figure 10. Equatorial inner edges of protons (red line) and electrons (blue line) of energies of 5 keV and 1 keV, respectively (thermal energies), at 20 R_E at midnight, under self-consistent (solid line) and T96 (dashed line) magnetic fields at (top) t = 10 h (after 4 h of enhanced, 90 kV, convection) and (bottom) t = 5 h (after 5 h of weak, 30 kV, convection).

Harang region. Their electric field measurements are made at r = 3.5–6 R_E, which is within the radial distances of our simulated Harang reversal in the equatorial plane, especially in the postmidnight region.

[43] Additionally, postmidnight storm time enhancement of ions of tens of keV observed by ENA [*Brandt et al.*, 2002] has been associated with the above described electric field skewing [*Ebihara and Fok*, 2004; *Buzulukova et al.*, 2010]. Therefore, it is important to understand how this skewing in the Harang region is affected by the SC magnetic field, and more specifically why the Harang in the SC run extends more toward dawn, something that would definitely affect the above postmidnight ion enhancements.

[44] In our previous study using the RCM simulations with T96 magnetic field model [*Gkioulidou et al.*, 2009], we have shown that the formation of the Harang reversal is a result of an overlap in the vicinity of midnight MLT of the R2 upward and downward FAC. In that overlap region, the downward FAC (located at lower latitudes) is associated with partial pressure peak of low-energy protons (~up to 400 eV at the midnight boundary) that penetrate closer to the Earth toward the dawn side, while the upward FAC (located at higher latitudes) is associated with the duskside bulk pressure peak of high-energy protons. Combining this understanding from our previous results with our current results, we can explain why the Harang reversal extends more toward dawn than in the SC run than in the T96 run. In Figure 11 we plot trajectories with solid contours and inner edge with red line for low-energy protons (400 eV at 20 R_E at midnight). It is clear that these low-energy protons, responsible for the downward FAC in the overlap region, penetrate closer to the Earth in the postmidnight sector in the SC run than in the T96 run, due to the reasons discussed in the previous section, that is, weaker shielding of the convection electric field. This means that the FAC overlap region extends more toward dawn and so does the Harang reversal, as can be clearly seen in Figure 7.

[45] The second phenomenon associated with the convection electric field is SAPS, which refers to the region of very strong tailward electric fields in the near-Earth premidnight sector. These strong SAPS electric fields are a result of ions penetrating to a region earthward of electrons where conductivity is low, so that a strongly enhanced electric field is required to maintain current continuity with the enhanced downward FAC in that region [*Southwood and*

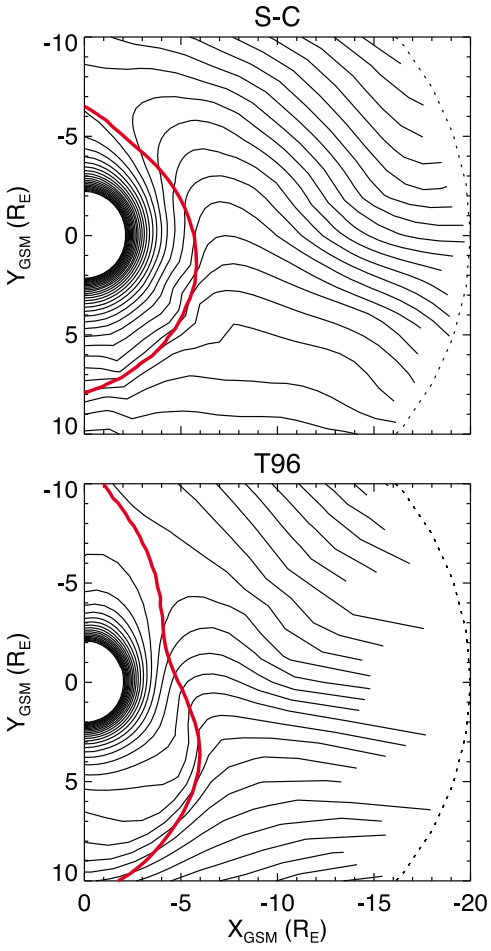

Figure 11. Proton trajectories with solid contours and inner edge for low-energy protons (400 eV at 20 R_E at midnight) with red lines at t = 6 h (convection has just reached 90 kV).

Wolf, 1978; *Anderson et al.*, 2001]. Therefore, the fact that the SAPS in the SC run ($X_{GSM} \sim -5\ R_E$ in the magnetosphere) is more confined in its radial (equatorial plane) and latitudinal (ionosphere) extent can be attributed to the premidnight inner edges of protons and electrons being located closer to each other than in the T96 run. The narrow latitudinal (1°–2°) and radial extend of the simulated SAPS in the SC run is also in better agreement with the observations both in the ionosphere, 64°–68° [*H. Wang et al.*, 2011], and in magnetosphere (<1 R_E) [*Nishimura et al.*, 2008].

4. Summary and Conclusions

[46] In this paper we have presented results from self-consistent simulations using the RCM coupled with a modified Dungey force-balanced magnetic field model. To investigate the role of the interplay between magnetic field and plasma sheet transport in the R2 coupling, we have compared our self-consistent RCM results (SC run) with the results from a RCM run using T96 magnetic field (T96 run).

[47] In the SC run, compared to the T96 model run, duskward magnetic drift is weaker for the thermal plasma sheet protons, which is the main contributor to plasma pressure, thus leading to weaker azimuthal pressure gradient in the inner magnetosphere. Since the gradient of flux tube volume is mainly directed radially, the weaker azimuthal pressure gradients result in weaker R2 FAC and thus less efficient electric field shielding in the near-Earth region. The less efficient shielding allows thermal plasma sheet protons to penetrate further earthward in the postmidnight sector. As a result, the inner edge of the these thermal protons is more azimuthally symmetric in the SC run, while in the T96 run there is a much more pronounced dawn-dusk asymmetry.

[48] Investigation of the inner edges of both protons and electrons shows that they are closer to each other and are more azimuthally symmetric in the SC run than in the T96 run. The electron inner edge is earthward (tailward) of the proton inner edge in the postmidnight (premidnight) sector and the two edges intersect at around midnight. Comparing weak convection to enhanced convection, the inner edges of both protons and electrons in the SC run become more azimuthally symmetric with increasing convection and are located even closer to each other. Also, the intersection of the ion and electron edges moves duskward under enhanced convection.

[49] The locations of the inner edges and the relative position between ion and electron edges determine the characteristics of the Harang reversal and the SAPS. More specifically, in the postmidnight sector, low-energy protons, which are responsible for the downward FAC of the overlapping FAC pair causing the Harang reversal, penetrate further toward dawn in the SC run because of less efficient shielding. This results in further dawnward extension of the Harang reversal. In the premidnight sector, the fact that the inner edges of protons and electrons are located closer to each other in the SC run causes the SAPS to be more confined in its radial and latitudinal width.

[50] We found that the magnitudes of the azimuthal pressure gradient, the inner edges of thermal protons and electrons, the latitudinal range of the Harang reversal, and the radial and latitudinal width of the SAPS become more consistent with observations when taking into account the feedback from force-balanced magnetic fields.

[51] **Acknowledgments.** The work by M.G. has been supported by NASA grants NNX07AF66G and NNX09AQ41H and by NSF grant ATM-0819864. The work by C.-P.W. and L.R.L. has been supported by NASA grants NNX07AF66G, NNX07AG42G, and NNX08A135G and by NSF grant ATM-0819864. The authors would like to thank R. A. Wolf and M. Schulz for very useful discussions.

[52] Masaki Fujimoto thanks the reviewers for their assistance in evaluating this paper.

References

Anderson, P. C., D. L. Carpenter, K. Tsuruda, T. Mukai, and F. J. Rich (2001), Multisatellite observations of rapid subauroral ion drifts (SAID), *J. Geophys. Res.*, *106*, 29,585–29,599, doi:10.1029/2001JA000128.

Brandt, P. C., S. Ohtani, D. G. Mitchell, M.-C. Fok, E. C. Roelof, and R. Demajistre (2002), Global ENA observations of the storm mainphase ring current: Implications for skewed electric fields in the inner magnetosphere, *Geophys. Res. Lett.*, *29*(20), 1954, doi:10.1029/2002GL015160.

Bristow, W. A., and P. Jensen (2007), A superposed epoch study of SuperDARN convection observations during substorms, *J. Geophys. Res.*, *112*, A06232, doi:10.1029/2006JA012049.

Buzulukova, N., M.-C. Fok, J. Goldstein, P. Valek, D. J. McComas, and P. C. Brandt (2010), Ring current dynamics in moderate and strong storms: Comparative analysis of TWINS and IMAGE/HENA data with the Comprehensive Ring Current Model, *J. Geophys. Res.*, *115*, A12234, doi:10.1029/2010JA015292.

Cahill, L., Jr. (1966), Inflation of the inner magnetosphere during a magnetic storm, *J. Geophys. Res.*, *71*, 4505–4519.

Chen, M. W., L. R. Lyons, and M. Schulz (1994), Simulations of phase space distributions of storm time proton ring current, *J. Geophys. Res.*, *99*, 5745–5759, doi:10.1029/93JA02771.

Dungey, J. W. (1963), The structure of the exosphere or adventures in velocity space, in *Geophysics: The Earth's Environment*, edited by C. DeWitt, J. Hieblot, and A. Lebeau, pp. 503–550, Gordon and Breach, London.

Ebihara, Y., and M.-C. Fok (2004), Postmidnight storm-time enhancement of tens-of-keV proton flux, *J. Geophys. Res.*, *109*, A12209, doi:10.1029/2004JA010523.

Gkioulidou, M., C.-P. Wang, L. R. Lyons, and R. A. Wolf (2009), Formation of the Harang reversal and its dependence on plasma sheet conditions: Rice convection model simulations, *J. Geophys. Res.*, *114*, A07204, doi:10.1029/2008JA013955.

Hesse, M., and J. Birn (1993), Three-dimensional magnetotail equilibria by numerical relaxation techniques, *J. Geophys. Res.*, *98*, 3973–3982, doi:10.1029/92JA02905.

Jordanova, V. K., S. Zaharia, and D. T. Welling (2010), Comparative study of ring current development using empirical, dipolar, and self-consistent magnetic field simulations, *J. Geophys. Res.*, *115*, A00J11, doi:10.1029/2010JA015671.

Le, G., C. Russell, and K. Takahashi (2004), Morphology of the ring current derived from magnetic field observations, *Ann. Geophys.*, *22*, 1267–1295.

Lemon, C., R. A. Wolf, T. W. Hill, S. Sazykin, R. W. Spiro, F. R. Toffoletto, J. Birn, and M. Hesse (2004), Magnetic storm ring current injection modeled with the Rice convection model and a self-consistent magnetic field, *Geophys. Res. Lett.*, *31*, L21801, doi:10.1029/2004GL020914.

Liu, S., M. W. Chen, M. Schulz, and L. R. Lyons (2006), Initial simulation results of storm-time ring current in a self-consistent magnetic field model, *J. Geophys. Res.*, *111*, A04225, doi:10.1029/2005JA011194.

Matsui, H., P. A. Puhl-Quinn, J. W. Bonnell, C. J. Farrugia, V. K. Jordanova, Y. V. Khotyaintsev, P.-A. Lindqvist, E. Georgescu, and R. B. Torbert (2010), Characteristics of storm time electric fields in the inner magnetosphere derived from Cluster data, *J. Geophys. Res.*, *115*, A11215, doi:10.1029/2010JA015450.

Nishimura, Y., J. Wygant, T. Ono, M. Iizima, A. Kumamoto, D. Brautigam, and R. Friedel (2008), SAPS measurements around the magnetic equator by CRRES, *Geophys. Res. Lett.*, *35*, L10104, doi:10.1029/2008GL033970.

Robinson, R. M., R. R. Vondrak, K. Miller, T. Dabbs, and D. Hardy (1987), On calculating ionospheric conductances from the flux and energy of precipitating electrons, *J. Geophys. Res.*, *92*, 2565–2569, doi:10.1029/JA092iA03p02565.

Schulz, M., and M. Chen (2008), Field-line (Euler-potential) model of the ring current, *J. Atmos. Sol. Terr. Phys.*, *70*, 482–489, doi:10.1016/j.jastp.2007.08.063.

Southwood, D. J., and R. A. Wolf (1978), An assessment of the role of precipitation in magnetospheric convection, *J. Geophys. Res.*, *83*, 5227–5232, doi:10.1029/JA083iA11p05227.

Stern, D. (1967), Geomagnetic Euler potentials, *J. Geophys. Res.*, *72*, 3995–4005.

Toffoletto, F. R., R. W. Spiro, R. A. Wolf, M. Hesse, and J. Birn (1996), Self-consistent modeling of inner magnetospheric convection, in *Third International Conference on Substorms (ICS-3)*, edited by E. J. Rolfe and B. Kaldeich, pp. 223–230, Eur. Space Agency, Noordwijk, Netherlands.

Toffoletto, F. R., J. Birn, M. Hesse, R. W. Spiro, and R. A. Wolf (2001), Modeling inner magnetospheric electrodynamics, in *Space Weather*, *Geophys. Monogr. Ser.*, vol. 125, edited by P. Song, H. Singer, and G. Siscoe, pp. 265–272, AGU, Washington, D. C.

Toffoletto, F., S. Sazykin, R. Spiro, and R. Wolf (2003), Inner magnetospheric modeling with the Rice convection model, *Space Sci. Rev.*, *107*, 175–196, doi:10.1023/A:1025532008047.

Tsyganenko, N. A. (1995), Modeling the Earth's magnetospheric magnetic field confined within a realistic magnetopause, *J. Geophys. Res.*, *100*, 5599–5612, doi:10.1029/94JA03193.

Tsyganenko, N. A. (1996), Effects of the solar wind conditions on the global magnetospheric configuration as deduced from data-based field models, *Eur. Space Agency Spec. Publ.*, *389*, 181–185.

Vasyliunas, V. M. (1970), Mathematical models of magnetospheric convections and its coupling to the ionosphere, in *Particles and Fields in the Magnetosphere*, edited by B. M. McCormac, pp. 60–71, D. Reidel, Hingham, Mass.

Wang, C.-P., L. R. Lyons, M. W. Chen, R. A. Wolf, and F. R. Toffoletto (2003), Modeling the inner plasma sheet protons and magnetic field under enhanced convection, *J. Geophys. Res.*, *108*(A2), 1074, doi:10.1029/2002JA009620.

Wang, C.-P., L. R. Lyons, T. Nagai, and J. C. Samson (2004), Midnight radial profiles of the quiet and growth-phase plasma sheet: The Geotail observations, *J. Geophys. Res.*, *109*, A12201, doi:10.1029/2004JA010590.

Wang, C.-P., L. R. Lyons, T. Nagai, J. M. Weygand, and R. W. McEntire (2007), Sources, transport, and distributions of plasma sheet ions and electrons and dependences on interplanetary parameters under northward interplanetary magnetic field, *J. Geophys. Res.*, *112*, A10224, doi:10.1029/2007JA012522.

Wang, C.-P., M. Gkioulidou, L. R. Lyons, R. A. Wolf, V. Angelopoulos, T. Nagai, J. M. Weygand, and A. T. Y. Lui (2011), Spatial distributions of ions and electrons from the plasma sheet to the inner magnetosphere: Comparisons between THEMIS-Geotail statistical results and the Rice convection model, *J. Geophys. Res.*, *116*, A11216, doi:10.1029/2011JA016809.

Wang, H., H. Lühr, K. Häusler, and P. Ritter (2011), Effect of subauroral polarization streams on the thermosphere: A statistical study, *J. Geophys. Res.*, *116*, A03312, doi:10.1029/2010JA016236.

Weimer, D. (1995), Models of high-latitude electric potentials derived with a least error fit of spherical harmonic coefficients, *J. Geophys. Res.*, *100*, 19,595–19,607, doi:10.1029/95JA01755.

Wolf, R. A. (1983), The quasi-static (slow-flow) region of the magnetosphere, in *Solar Terrestrial Physics*, edited by R. L. Carovillano and J. M. Forbes, pp. 303–368, D. Reidel, Hingham, Mass.

Xing, X., L. R. Lyons, V. Angelopoulos, D. Larson, J. McFadden, C. Carlson, A. Runov, and U. Auster (2009), Azimuthal plasma pressure gradient in quiet time plasma sheet, *Geophys. Res. Lett.*, *36*, L14105, doi:10.1029/2009GL038881.

Yang, J., F. R. Toffoletto, and Y. Song (2010), Role of depleted flux tubes in steady magnetospheric convection: Results of RCM-E simulations, *J. Geophys. Res.*, *115*, A00I11, doi:10.1029/2010JA015731.

Zaharia, S. (2008), Improved Euler potential method for three-dimensional magnetospheric equilibrium, *J. Geophys. Res.*, *113*, A08221, doi:10.1029/2008JA013325.

Zaharia, S., C. Z. Cheng, and K. Maezawa (2004), 3-D force-balanced magnetospheric configurations, *Ann. Geophys.*, *22*, 251–265, doi:10.5194/angeo-22-251-2004.

Zou, S., L. R. Lyons, C.-P. Wang, A. Boudouridis, J. Ruohoniemi, P. Anderson, P. Dyson, and J. Devlin (2009), On the coupling between the Harang reversal evolution and substorm dynamics: A synthesis of SuperDARN, DMSP and IMAGE observations, *J. Geophys. Res.*, *114*, A01205, doi:10.1029/2008JA013449.

M. Gkioulidou, L. R. Lyons, and C.-P. Wang, Department of Atmospheric and Oceanic Sciences, University of California, Los Angeles, CA 90095, USA. (mgioul@atmos.ucla.edu)